Top of the Atmosphere Reflected Shortwave Radiative Fluxes from GOES-R

Rachel T. Pinker[1], Yingtao Ma[1], Wen. Chen[1], Istvan Laszlo[2], Hongqing Liu[3], Hye-Yun Kim[3] and Jamie Daniels[2]

[1] Department of Atmospheric and Oceanic Science, University of Maryland, College Park, MD

[2] NOAA NESDIS Center for Satellite Applications and Research, College Park, MD

[3]I.M. Systems Group, Inc., Rockville, MD

Correspondence to: Rachel T. Pinker (pinker@atmos.umd.edu)

Abstract. Under the GOES-R activity, new algorithms are being developed at the National Oceanic and Atmospheric Administration (NOAA)/Center for Satellite Applications and Research (STAR) to derive surface and Top of the Atmosphere (TOA) shortwave (SW) radiative fluxes from the Advanced Baseline Imager (ABI), the primary instrument on GOES-R. This paper describes a support effort in the development and evaluation of the ABI instrument capabilities to derive such fluxes. Specifically, scene dependent narrow-to-broadband (NTB) transformations are developed to facilitate the use of observations from ABI at the TOA. Simulations of NTB transformations have been performed with MODTRAN4.3 using an updated selection of atmospheric profiles and implemented with the final ABI specifications. These are combined with Angular Distribution Models (ADMs), which are a synergy of ADMs from the Clouds and the Earth's Radiant Energy System (CERES) and from simulations. Surface condition at the scale of the ABI products as needed to compute the TOA radiative fluxes come from the International Geosphere-Biosphere Programme (IGBP). Land classification at 1/6 ^{o} resolution for 18 surface types are converted to the ABI 2-km grid over the (CONtiguous States of the United States) (CONUS) and subsequently re-grouped to 12 IGBP types to match the classification of the CERES ADMs. In the simulations, default information on aerosols and clouds is based on the ones used in MODTRAN.

Comparison of derived fluxes at the TOA is made with those from CERES and the level of agreement for both clear and cloudy conditions is documented. Possible reasons for differences are discussed. The product is archived and can be downloaded from the NOAA Comprehensive Large Array-data Stewardship System (CLASS).

Introduction

One of the objectives at NOAA/STAR in respect to the utilization of observations from the Advanced Baseline Imager (ABI) is to be able to derive shortwave (SW↓) radiative fluxes at the surface. To get to the surface SW↓ from TOA satellite observations, there are two generic approaches: 1) the direct approach and 2) the indirect approach. In the direct approach one uses all the necessary information needed for deriving the surface fluxes (some of which can be derived from satellites). Implementation of such an approach is feasible, for instance, with observations from MODIS which has a long history of product availability and evaluation. Examples are illustrated in Wang and Pinker (2009), Niu and Pinker, (2015), Ma et al. (2016), Pinker et al. (2018), Pinker et al., (2017a), Pinker et al. (2017b). GOES-R is a new instrument and as yet, similar information to the one from MODIS is not yet available. Therefore, the indirect approach is used where one starts from satellite observations at the TOA and models the atmosphere and surface with best available information (which does not have to be based on ABI). Examples of such an approach are discussed in Pinker, Zhang and Dutton (2005), Ma and Pinker (2012) and Zhang et al. (2019). The "indirect path method" is used at the Center for Satellite Applications and Research (STAR) (Laszlo et al., 2020) for deriving SW↓ radiative fluxes from satellite observations; it requires knowledge of the SW broadband (0.2 – 4.0 μm) top of the atmosphere (TOA) albedo. The Advanced Baseline Imager (ABI) observations onboard of the NOAA GOES-R series of satellites provide reflectance in six narrow bands in the shortwave spectrum (**Table 1**); these must be first transformed into broadband reflectance (the NTB conversion), and the broadband reflectance must be transformed into a broadband albedo (the ADM conversion). During the pre-launch activity NTB transformations were developed based on theoretical radiative transfer simulations with MODTRAN-3.7 and 14 land use

classifications from the International Geosphere-Biosphere Programme (*IGBP) (*Hansen et al., 2010*).* They were augmented with ADMs from (CERES) observed ADMs (Loeb et al., 2003) and theoretical simulations (Niu and Pinker, 2011) to compute TOA fluxes. The resulting NTB transformations and ADMs have been tested using proxy data and simulated ABI data. The proxy instruments used in these early simulations include the GOES-8 satellite, the Advanced Very-High Resolution Radiometer (AVHRR) sensor on the Polar Orbiting satellites, the Spinning Enhanced Visible Infra-Red Imager **(**SEVIRI) sensor on the European METEOSAT Second Generation (MSG) satellites, and the Moderate Resolution Imaging Spectroradiometer (MODIS) instrument on the NASA Terra and Aqua Polar Orbiting satellites (Pinker et al., 2021, unpublished). For each of these satellites, the evaluation of the methodologies was done differently; some results were evaluated against ground observations while others, against TOA information from CERES as well as from the (ESA) Geostationary Earth Radiation Budget (GERB) satellite (Harries et al., 2005). The results obtained provided an insight on the expected performance of the new ABI sensor. Those procedures have been subsequently updated and applied to the new ABI instrument once it was built and fully characterized.

In this paper we describe activity in support of the effort to derive surface shortwave (SW↓) radiative fluxes from the operational Advanced Baseline Imager (ABI) instrument on the GOES-R series of the NOAA geostationary meteorological satellites using the latest version of the ABI data. We describe the physical basis and the development of the (NTB) transformations of satellite observed radiances and the bi-directional corrections to be applied to the broadband reflectance to obtain broadband TOA albedo. The methodology will be presented in section 2, data used are described in section 3, results in section 4 and a summary and discussion in section 5.

2. Methodology

The following two flowcharts (**Figs. 1 and 2**) describe the necessary steps to derive the NTB transformations and the ADMs. Details on these two steps will follow.

The TOA narrowband and broadband reflectance can be calculated from the spectral radiances simulated from MODTRAN 4.3 and the response functions of the satellite sensor as shown in equations (1) and (2):

$$\rho_{nb}(\theta_0,\theta,\phi)=\frac{\pi\int_{\lambda 1}^{\lambda 2} I(\lambda,\theta_0,\theta,\phi)G(\lambda)d\lambda}{\int_{\lambda 1}^{\lambda 2}\cos(\theta_0)S_0(\lambda)G(\lambda)d\lambda} \quad (1)$$

$$\rho_{bb}(\theta_0,\theta,\phi)=\frac{\pi\int_{0.2\mu m}^{4\mu m} I(\lambda,\theta_0,\theta,\phi)d\lambda}{\int_{0.2\mu m}^{4\mu m}\cos(\theta_0)S_0(\lambda)d\lambda} \quad (2)$$

where ρ_{nb} is narrowband reflectance; ρ_{bb} is broadband reflectance; θ_0: solar zenith angle; θ: view (satellite) zenith angle; ϕ: relative azimuth angle;

I_λ: reflected spectral radiance; $S_0(\lambda)$: solar spectral irradiance;

G_λ: spectral response functions of satellite sensors; λ_1 and λ_2 are the spectral limits of the sensor spectral band. This approach is widely used in the scientific community as also implemented in the work of Loeb et al (2005), Wielicki et al. (2008), Su et al. (2015) and Akkermans et al. (2020).

As stated previously, the ADMs from CERES-based observations (Loeb et al., 2005; Kato et al. 2015) were augmented with theoretical simulations (Niu and Pinker, 2011) to compute TOA fluxes. This was done since CERES observations at that time were under-sampled at higher latitudes.

The combined ADMs are developed for each angular bin by weighting the modeled and CERES ADMs based on the number of samples used to derive the ADMs of each type (Niu et al., 2011). Specifically:

$$\bar{R}(\theta_0,\theta,\phi) = \frac{1}{m+n}\left(m \times R_{CERES}(\theta_0,\theta,\phi) + n \times R_S(\theta_0,\theta,\phi)\right) \quad (3)$$

$\bar{R}(\theta_0,\theta,\phi)$: averaged ADMs at each angular bin;

R_{CERES}: anisotropic factor from CERES ADMs;

R_S: anisotropic factor from simulated ADMs;

m and *n*: observation numbers at angular bins for CERES and simulated ADMs.

2.1 Selection of Atmospheric profiles for simulations

We have selected 100 atmospheric profiles covering the globe and the seasons as input for simulations with MODTRAN4.3. The atmospheric profiles at each pressure level include temperature, water vapor and ozone. Each season includes 25 profiles. A tool was developed to select profiles from a Training Data set known as SeeBor Version 5.0 (https://cimss.ssec.wisc.edu/training_data/) (Borbas et.al. 2005). Originally it consisted of 15704 global profiles of temperature, moisture, and ozone at 101 pressure levels for clear sky conditions. The profiles are taken from NOAA-88, and the European Centre for Medium-Range Weather Forecasts (ECMWF) 60L training set, TIGR-3, ozone-sondes from 8 NOAA Climate Monitoring and Diagnostics Laboratory (CMDL) sites, and radiosondes from the Sahara Desert during 2004. A technique to extend the temperature, moisture, and ozone profiles above the level of existing data was also implemented by the providers (University of Wisconsin-Madison, Space Science and Engineering Center, Cooperative Institute for Meteorological Satellite Studies (CIMSS). **Fig. 3** shows the location of the selected profiles.

The SeeBor profiles are clear sky profiles. The top of the profiles is at 0.005 mb which is about 82.6 km. We did an experiment to check the impact of reducing the number of levels for a profile (initially, we have used only 40 levels). In the experiment computed were radiances from profiles with 50 levels as

well as radiances from profiles with 98 Levels. The difference between the two radiances (50 lev-98 lev) were below 5 % reaching 15 % around 2.5 μm. In the experiment we used the odd number levels starting from surface (plus the highest level) to reduce the number of profile levels. Based on these experiments we have opted to keep all 98 profile levels.

The surface variables we have used are from MODIS and include surface skin temperature, 2 m temperature, land/sea mask, and albedo. We have conducted a thorough investigation how the selected profiles represent the entire sample of 15704 profiles. An example showing the comparison of temperature, humidity and ozone profiles is shown in **Fig. 4.** As seen, there is a positive bias in the selected profile of temperature due to their higher concentration at the lower latitudes. A positive bias can be found at the lower levels while a negative bias is seen above 1 mb. Since our domain of study is in such latitudes this selection should not have adverse effects on the simulations performed.

2.2 Surface conditions

Surface condition is one of the primary inputs into the MODTRAN simulations. The International Geosphere-Biosphere Programme (IGBP) land classification is used as a source (Hansen et al., 2010; Loveland et al., 2010). The dataset is at 1/6-degree resolution and includes 18 surface types. We have converted the $1/6^{o}$ (~18.5 km) resolution to the ABI 2-km grid using the nearest grid method **(Fig. 5**). The surface type is fixed in time. The method for cloudy sky uses 4 surface types; these are also derived from 12 IGBP types (**Table 2**).

2.3 Clear and cloudy sky simulations

Under clear sky, scattering from aerosols is important. We have included 6 aerosol types (**Table 3**) to cover a range of possible conditions under clear sky. Aerosol models are selected based on the type of extinction and a default meteorological range for the boundary-layer aerosol models as listed below:

Aerosol Type 1: Rural extinction, visibility = 23 km

Aerosol Type 4: Maritime extinction, visibility = 23 km

Aerosol Type 5: Urban extinction, visibility = 5 km

Aerosol Type 6: Tropospheric extinction, visibility = 50 km

Aerosol Type 8: Advective Fog extinction, visibility = 0.2 km

Aerosol Type 10: Desert extinction for default wind conditions

For the 6 aerosol types, the total number of MODTRAN simulations for each surface type is 462,000. It is obtained as follows: 6 aerosol types x 100 profiles x 770 angles.

When performing NTB simulations, we use all 6 types of aerosols. The Rural, Ocean, Urban and Fog aerosols are distributed in the lower 0-2 km region. Tropospheric aerosol is distributed from 0 to 10 km tropopause. The Rural, Ocean, Urban and Tropospheric aerosol optical properties have Relative Humidity (RH) dependency. The Single Scattering Albedo (SSA) is given on 4 RH grids (0, 70, 80, 99) on a spectral grid of 788 points ranging from 0.2 to 300 microns.

Simulations were performed for ABI for all the cloud cases described in **Table 3.** To merge cloud layers with atmospheric profiles we have followed the procedure as described in *Berk et al.* (1985, 1998), namely: "Cloud profiles are merged with the other atmospheric profiles (pressure, temperature, molecular constituent, and aerosol) by combining and/or adding new layer boundaries. Any cloud layer boundary within half a meter of an atmospheric boundary layer is translated to make the layer altitudes coincide; new atmospheric layer boundaries are defined to accommodate the additional cloud layer boundaries." 100% relative humidity is assumed within the cloud layers (default).

2.4 Selection of angles

The total number of angles used in the simulations is given in **Table 4**. The selected spectral grids for solar zenith angles, satellite view angles and relative azimuth angles are at Gaussian quadrature points, plus 0^o to solar zenith angles (sza) and satellite viewing angles (vza) and 0^o and 180^o (forward and backward view) to the satellite relative azimuth angles. Solar angle and satellite view angle are referenced

to target or surface for satellite simulation with 0^o meaning looking up (zenith). Relative azimuth angle is defined as when the relative azimuth angle equals 180^o, the sun is in front of observer.

The definitions of solar zenith angle and azimuth angle in this table corresponds to the definitions of MODTRAN but that is not the case for the satellite zenith angle. MODTRAN uses nadir angle as 180^o-satellite zenith angle, ignoring spherical geometry.

2.5 Selection of optimal computational scheme

MODTRAN4.3 provides three multiple scattering models (Isaacs, DISORT, and Scaled Isaacs) and three band models at resolutions (1 cm^{-1}, 5 cm^{-1}, and 15 cm^{-1}). The DISORT model (Stamnes et al., 1988) provides the most accurate radiance simulations but the runs are very time consuming. The Isaacs (Isaacs et al. 1987) 2-stream algorithm is fast but oversimplified. The Scaled Isaacs method performs radiance calculations using Isaacs 2-stream model over full spectral range and using DISORT model at a small number of atmospheric window wavelengths. The multiple scattering contributions for each method are identified and ratios of the DISORT and Isaacs methods are computed. This ratio is interpolated over the full wavelength range, and finally, applied as a multiple scattering scale factor in a spectral radiance calculation performed with the Isaacs method.

To optimize simulation speed and accuracy, we performed various sensitivity tests, including combinations of multiple scattering models, band resolution, and number of streams. **Table 5** lists simulation options and their corresponding calculation speed.

Based on results presented in **Table 5**, the efficient options (< 40 seconds) are Isaacs, DISORT 2-stream with 15 cm^{-1}, DISORT 4-stream 15 cm^{-1}, and Scaled Isaacs all streams at all resolutions. Although the ideal option is DISORT 8-stream with 1 cm^{-1} resolution, there is a trade-off between speed and accuracy. **Fig. 6** compares DISORT simulated radiances at three band resolutions. We use two spectral ranges of 0.4 – 0.5 μm and 1.5 – 2.0 μm to illustrate differences. **Fig. 6** shows that the coarser band resolution has smoothed out the radiance variations. The 15 cm^{-1} has the smoothest curve among the three, and 1 cm^{-1} shows more variations than the other two. Another (scientific) criteria for selecting the spectral resolution

is the ability to resolve/match the relative spectral response function (SRF) of a sensor. For example, the SRFs of channels 1-6 of ABI are given at every 1 cm^{-1}.

Accordingly, we have chosen the 1 cm^{-1} band model for the MODTRAN radiance simulations. Performed were also radiance simulations from different multiple scattering models at 1 cm^{-1} resolution. The whole spectrum of 0.2 – 4 μm was separated to 14 sections so that the differences can be assessed clearly. For wavelength below 0.3 μm and beyond 2.5 no discernible differences were found among Isaacs, DISORT 2-, 4-, and 8-strem, and Scaled Isaac. The largest differences occurred in the spectral range of 0.4 – 1.0 μm. Scaled Isaac 8-stream follows DISORT 8-stream closely across the whole spectral range; the Scaled Isaac method provided near-DISORT accuracy with the speed of Isaacs. Thus, the MODTRAN4.3 simulations for GOES-R ABI were set-up with Scaled Isaac 8-stream with 1 cm^{-1} band resolution.

For illustration, in **Fig. 7** compared are radiances simulated by Isaac 2 stream, Scaled Isaac, and DISORT-4 stream for the case of Relative Azimuthal Angle=1.9^o, View Angle=76.3^o, Solar Zenith Angle=87.2^o. The lines are differences between various settings and DISORT-8 stream (e.g. Isaacs minus DISORT-8). Isaac has the least accuracy since it is oversimplified, 4-stream showed some improvements when compared with Isaac while still has large differences for 0.4 μm and is still computationally demanding. Scaled Isaac provides the smallest differences between DISORT-8. **Fig. 7** (lower) zoomed in to the large difference area of 0.3-0.35 μm which indicates that Scaled Isaacs still provides satisfactory results.

2.6 Regression methodologies

We have derived coefficients of regression using a constrained least-square curve fitting methods of Matlab, “lsqnonneg”, which can solve a linear or nonlinear least-squares (data-fitting) problem and produce non-negative coefficients. Non-negative coefficients avoid generating negative TOA flux, which is not a physically valid.

To ensure that information from all channels is used and avoid the complex cross-correlation problem, it was opted to generate Narrow to Broad (NTB) coefficients for each ABI channel separately. These channel specific NTB coefficients are applied to each channel to convert ABI narrow-band reflectance to

extended band. The final broad-band TOA reflectance is taken as the weighted sum of all 6-channel specific broad-band reflectance. The logic behind this approach is the assumption that the narrow-band reflectance from each channel is a good representative for a limited spectral region centered around the channel and the total spectral reflectance is dominated by the spectral region that contains the most solar energy.

To generate "separate-channel" NTB coefficients, each narrow-band ABI channel reflectance is converted to a reflectance $\rho_{bb,i}$ separately,

$$\rho_{bb,i}(\theta_0,\theta,\phi) = c_{0,i}(\theta_0,\theta,\phi) + c_{1,i}(\theta_0,\theta,\phi) * \rho_{nb,i}\,(\theta_0,\theta,\phi) \quad (4)$$

where $\rho_{bb,i}$ is the band reflectance for an interval around each channel i; $c_{0,i}$ and $c_{1,i}$ are regression coefficients for channel i. These regression coefficients are derived separately for various combination of surface, cloud and aerosol types. The total shortwave broad band (0.25 – 4.0μm) reflectance ρ_{bb}^{est} is obtained by taking the weighted sum of all 6 $\rho_{bb,i}$ reflectance

$$\rho_{bb}^{est}(\theta_0,\theta,\phi) = \sum_i \rho_{bb,i}(\theta_0,\theta,\phi)\frac{S_{0,i}}{S_0} \quad (5)$$

Here, S_0 and $S_{0,i}$ are total solar irradiance and band solar irradiance for each channel, respectively. Band edges around the six ABI channels are: 49980-18723, 18723-13185, 13185-9221, 9221-6812, 6812-5292, 2500 cm^{-1} 0.2001-0.5341, 0.5341-0.7584, 0.7584-1.0845, 1.0845-1.4680, 1.4680-1.8896, 1.8896-4.0000 μm). The corresponding solar irradiance band values are 364, 360, 287, 168, 91, 87 W m^{-2}. **Fig. 8** shows the sensor response function (SRF) and locations of the six ABI channels.

Coefficients are generated for clear condition and 3 types of cloudy conditions. Comparison between ABI TOA flux and CERES products are shown in **Fig. 9**. The "separate-channel" coefficients work well for predominantly clear sky (**Fig.10**). Differences are somewhat more scattered for cloudy cases. The reason may be due to the fact that the ABI observation time and CERES product time do not match perfectly since cloud condition change quickly. As discussed in Gristey et al. (2019) there are SW spectral reflectance variations for different cloud types. Possibly, for ABI bands some spectral variations associated with cloud variability are missed. It is important to have the correct cloud properties to be able to select correct ADM. Misclassification of cloud properties will therefore result in flux differences. They

also argue that ADMs have an uncertainty due to within-scene variability and within-angular bin variability leading to additional flux differences.

3. Data used

3.1 Satellite data for GOES-16 and GOES17

The GOES Imager data used **(Table 6)** were downloaded from https://www.avl.class.noaa.gov/saa/products/welcome. When searching the NOAA CLASS site, go to "GOES-R Series ABI Products GRABIPRD (partially restricted L1b and L2+ Data Products)". The SRF are downloaded from https://ncc.nesdis.noaa.gov/GOESR/ABI.php.

3.2 Reference data from CERES

The CERES Single Scanner Footprint (SSF) is a unique product for studying the role of clouds, aerosols, and radiation in climate. Each CERES footprint (nadir resolution 20-km equivalent diameter) on the SSF includes reflected shortwave (SW), emitted longwave (LW) and window (WN) radiances and top-of-atmosphere (TOA) fluxes from CERES with temporally and spatially coincident imager-based radiances, cloud properties, and aerosols, and meteorological information from a fixed 4-dimensional analysis provided by the Global Modeling and Assimilation Office (GMAO). Each file in this data product contains one hour of full and partial-Earth view measurements or footprints at a surface reference level. Detailed information can be found via https://ceres.larc.nasa.gov/data/#ssf-level-2 (we used version 4a) Near real-time CERES fluxes and clouds in the SSF format are available within about a week of observation (Kratz et al., 2014). They do not use the most recent CERES instrument calibration and thus contains some uncertainty. Before GOES data were transferred to the Comprehensive Large Array-data

Stewardship System (CLASS) system, the NOAA/STAR archive was holding new data for about a week. Therefore, the initial evaluations had to be done only with data that overlapped in time. The CERES data known as the FLASHFlux Level2 (FLASH_SSF) are available almost in real time from: https://ceres.larc.nasa.gov/products.php?product=FLASHFlux-Level2 (we used version 3c). Due to such constraints the early comparison was done between ABI data as archived at NOAA/STAR and the FLASHFlux products (in this paper, the FLASHFlux data were used only in Fig. 9). The archiving of GOES-R at the NOAA Comprehensive Large Array-data Stewardship System (CLASS) started only in 2019, however, it contains data starting from 2017. Once the CLASS archive became available, we have augmented GOES-16 cases with observations from GOES-17; only those cases will be shown in this paper.

3.3 Data preparation

For the re-mapping, we adopted the ESMF re-gridding package. The detailed information can be found at: http://earthsystemmodeling.org/regrid/

For an ideal situation, the ABI high-resolution TOA SW fluxes should be mapped into the CERES footprint for validation. However, there are reasons that make it difficult to do so. There can be more than 18000 pixels in a single swath of the SSF, when constrained to U.S. Different pixels have different times. Neglecting the seconds, there are still more than 30 mins differences (this changes case by case) between the first pixel and the one at the end and this brings up a time matching issue. By remapping the SSF to

ABI, we can set up a unique time for ABI (ABI is at 5 min intervals) and then constrain the region and the time range of SSF.

Both re-mapping the ABI to SSF and remapping SSF to the ABI bring up spatial matching errors as recognized by the scientific community (Rilee and Kuo, 2018; Ragulapati et al., 2021). In **Fig. 11**, we show the SSF before re-gridding (**Figs 11 (a) & (b)**) and after re-gridding (**Figs. 11 (c) and (d)).** The fluxes after re-mapping CERES SSF to the ABI resolution resemble well the original structure. Another consideration is the computational efficiency of re-mapping the curvilinear tripolar grid to unconstructed grid. For large arrays, it is more efficient to remap the unconstructed grid to the curvilinear tripolar grid.

4. Results

4.1 Comparison between ABI TOA fluxes to those from CERES SSF

A case for 2019/12/26 (doy 360) UTC 19:36 is illustrated in **Figs. 11-14.** Statistical summaries from an extended number of cases that cover all four seasons are presented in **Table 7**.

We have conducted several experiments to select an appropriate regression approach to the NTB transformation ensuring that non-physical results are not encountered. Based on the samples used in this study **(Table 7)** the differences found for Terra and GOES-16 were in the range of -0.5-(-17.37) for bias and 43.28-81.72 for standard deviation; for Terra and GOES-17 they were 11.26-47.09 and 70.25-108.73, respectively. For Aqua and GOES-16 they were 7.63-33.87and 58.68-117.43 respectively while for Aqua and GOES-17 they were 0.19-31.53 and 47.55-129.42, respectively (all units are W m^{-2}). The evaluation process revealed the challenges in undertaking such comparisons. Both estimates of TOA fluxes (CERES and GOES) do no account for seasonality in the land use classification; the time matching for the different satellites is important and limits the number of samples that can be used in the comparison. Based on the results of this study recommendation for future work include the need to incorporate seasonality in land

use and spectral characteristic of the various surface types. Possible stratification by season in the regressions could also be explored.

4.2 Causes for differences between ABI and CERES TOA fluxes

4.2.1 Differences in surface spectral reflectance

In the MODTRAN simulations we use the spectral reflectance information on various surface types as provided by MODTRAN. MODTRAN version 4.3.1 contains a collection of spectral surface reflectance dataset from the Moderate Spectral Atmospheric Radiance and Transmittance (MOSART) model (Cornette et al., 1994) and others from Johns Hopkins University Spectral Library (Baldridge et al., 2009). When doing simulation, we call the built-in surface types and use the provided surface reflectance. As such, the spectral dependence of the surface reflectance used in the simulations and matched to the CERES surface types may not be compatible with the classification of CERES. Also, seasonal changes in surface type classification can introduce errors due to changes in the spectral surface reflectance for different surface types (**Fig. 15).**

4.2.2 Issues related to surface classification

Another possible cause for differences between the TOA fluxes is the classification of surface types as originally identified by the IGBP and used in the simulations. No seasonality is incorporated in the surface type classification while such variability is part of the CERES observations.

4.2.3 Issues related to match-up between GOES-R and CERES

Both Terra and Aqua have sun-synchronous, near-polar circular orbits. Terra is timed to cross the equator from north to south (descending node) at approximately 10:30 am local time. Aqua is timed to cross the

equator from south to north (ascending node) at approximately 1:30 pm local time. The periods for Terra and Aqua are 99 and 98 minutes, respectively. Both have 16 orbits per day. CERES on Terra and Aqua optical FOV at nadir is 16 x 32 or 20 km resolution. Terra passes CONUS during 03-06 UTC (US night time), 16-20 UTC (US day time), and Aqua passes CONUS during 07-11 UTC (US night time), 18-22 UTC (US day time).

Both Terra and Aqua have an instantaneous FOV values at SWATH level. There is no perfect overlap, temporally or spatially with ABI data. The ABI radiance and cloud data are on a regular grid of 2*2 km over CONUS at each hour. To use CERES data for evaluation of ABI, there is a need to perform collocation in both time and space.

5. Summary

The derivation and evaluation of TOA radiative fluxes as simulated for any given instrument are quite challenging. In principle, there is a need to account for all possible changes in the atmospheric and surface conditions one may encounter in the future. Yet, to know what these conditions are at the time of actual observation when there is a need to select the appropriate combination of variables from the simulations, is a formidable task. Differences in assumed cloud properties can also lead to differences in the fluxes derived from the two instruments. Therefore, error can be expected due to discrepancies between the actual conditions and the selected simulations and these are difficult to estimate. The approach we have selected is based on high-quality simulations using a proven and accepted radiative transfer code (MODTRAN) of known configurations and a wide range of atmospheric conditions. We have also selected the best available estimates of TOA radiative fluxes from independent sources for evaluation. However, the matching between different satellites in space and time is challenging. In selecting the cases for evaluation, we have adhered to strict criteria of time and space coincidence as described in section 3.3.

Critical elements of an inference scheme for TOA radiative flux estimates from satellite observations are:

1) transformation of narrowband quantities into broadband ones;

2) transformation of bi-directional reflectance into albedo by applying Angular Distribution Models (ADMs). In principle, the order in which these transformations are executed is arbitrary. However, since well established, observation-based broadband ADMs derived from the Clouds and the Earth's Radiant Energy System (CERES) project already exist, the logical procedure is to do the NTB transformation on the radiances first, and then apply the ADM. This is the sequence that has been followed here. While the road map to accomplish above objectives seems well defined, reaching the final goal of having a stable up-to-date procedure for deriving TOA radiative fluxes from a new instrument like the ABI on the new generation of GOES satellites is quite complicated. Since the final configuration of the instrument becomes known at a much later stages the evaluation of new algorithms is in a fluid stage for a long time so early evaluation against "ground truth" needs to be repeated frequently. Additional complication is related to the lack of maturity of basic information needed in the implementation process, such as a reliable cloud screened product which in itself is in a process of development and modifications. The "ground truth", namely, the CERES observations are also undergoing adjustments and recalibration. As such, the process of deriving best possible estimates of TOA radiative fluxes from ABI underwent numerous iterations to reach its current status. An effort was made to deal the best way possible with the fluid situation. All the evaluations against CERES were repeated once the ABI data reached stability and were archived in CLASS and we used the most recent auxiliary information. This study sets the stage for future possible improvements. One example is land classification which currently is static. Another issue is related to the representation of real time aerosol optical properties which are important under clear sky conditions. It is believed that only now when NOAA/STAR has a stable aerosol retrieval algorithm, it would be timely to address the aerosol issue in the estimation of TOA fluxes under clear sky.

Data availability. The data are available upon request from the corresponding author.

Author contributions. The investigation and conceptualization were carried out by RTP, IL and JD. YM and WC developed the software. RTP prepared the original draft. All authors contributed to the writing, editing and review of the publication.

Competing interests. The authors declare that they have no conflict of interest.

Disclaimer. Publisher's note: Copernicus Publications remains neutral with regard to jurisdictional claims in published maps and institutional affiliations.

Acknowledgements. We acknowledge the benefit from the use of the numerous data sources used in this study. These include the Clouds and the Earth's Radiant Energy System (CERES) teams, the Fast Longwave and Shortwave Radiative Flux (FLASHFlux) teams, the
University of Wisconsin-Madison, Space Science and Engineering Center, Cooperative Institute for Meteorological Satellite Studies (CIMSS) for providing the SeeBor Version 5.0 data (https://cimss.ssec.wisc.edu/training_data/, and the final versions of the GOES Imager data were downloaded from https://www.bou.class.noaa.gov/. Several individuals have been involved in the early stages of the project whose contribution led to the refinements of the methodologies. These include M. M. Woncsick and Shuyan Liu. We thank the anonymous Reviewers for a very thorough and constructive comments that helped to improve the manuscript. We thank the Editor Sebastian Schmidt for overseeing the disposition of the manuscript.

Financial support. This research was supported by NOAA/NESDIS GOES-R Program under grants 5275562 1RPRP_DASR and 275562 RPRP_DASR_20 to the University of Maryland.

Reference:

Akkermans T., and Clerbaux, N.: Narrowband-to-Broadband Conversions for Top-of-Atmosphere Reflectance from the Advanced Very High-Resolution Radiometer (AVHRR), Remote Sens. 12 (2), 305; https://doi.org/10.3390/rs12020305, 2020.

Berk, A., Bernstein, L. W., and Robertson, D. C.: MODTRAN: A moderate resolution model for LOWTRAN 7, Philips Laboratory, Report AFGL-TR-83-0187, Hanscom AFB, MA, 1985.

Berk, A., G. P. Anderson, P. K., Acharya, D. C. Robertson, J. H. Chetwynd, S. M. Adler-Golden: MODTRAN Cloud and Multiple Scattering Upgrades with Application to AVIRIS, Remote Sensing of Environment, 65 (3), 367-375, https://doi.org/10.1016/S0034-4257(98)00045-5, 1998.

Baldridge, A. M., Hook, S. J., Grove, C. I., Rivera, G.: The ASTER spectral library version 2, Remote Sensing of Environment 113, doi: 10.1016/j.rse.2008.11.007, 2009.

Borbas, E. E., Seemann, S. W., Huang, H.-L., Li, J., and Menzel, W. P.: Global profile training database for satellite regression retrievals with estimates of skin temperature and emissivity. Proceedings of the XIV, International ATOVS Study Conference, Beijing, China, University of Wisconsin-Madison, Space Science and Engineering Center, Cooperative Institute for Meteorological Satellite Studies (CIMSS), Madison, WI, pp.763-770, 2005.

Clerbaux, N., Russell, J. E., Dewitte, S., Bertrand, C., Caprion, D., De Paepe, B., Sotelino, L. G., Ipe, A., Bantges, R., and Brindley, H. E.: Comparison of GERB instantaneous radiance and flux products with CERES Edition-2 data, Rem. Sens. of Environ., **113**, 102-114. doi: 10.1016/j.rse.2008.08.016, 2009.

Cornette, W. M., Acharya, P. K., Robertson, D. C., and Anderson, G. P.: Moderate Spectral Atmospheric Radiance and Transmittance Code *(MOSART)*, Rep. R-057-94 (11–30), La Jolla, CA: Photon Research Associates, 1994.

Gristey, J. J., Su, W., Loeb, N. G., Vonder Haar, T. H., Tornow, F., Schmidt, K. S., Hakuba, M. Z.,

Pilewskie, P., Russell, J. E.: Shortwave Radiance to Irradiance Conversion for Earth Radiation Budget Satellite Observations: A Review, Remote Sens. 13, 2640, https://doi.org/10.3390/rs13132640, 2021.

Kato, S., Loeb, N. G., Rutan, D. A., Rose, F. G.: Clouds and the Earth's Radiant Energy System (CERES) Data Products for Climate Research Journal of the Meteorological Society of Japan, 93 (6), 597−612, DOI:10.2151/jmsj.2015-048, 2015.

Kratz, D. P., Stackhouse Jr., P. W., Gupta, S. K., Wilber, A. C., Sawaengphokhai, P., and McGarragh, G. R.: The Fast Longwave and Shortwave Flux (FLASHFlux) Data Product: Single-Scanner Footprint Fluxes, J. Appl. Meteor. Climatology, 53, 1059-1079, doi: 10.1175/JAMC-D-13-061.1, 2014.

Hansen, M. C., Defries, R. S., Townshend, J. R. G., and Sohlberg, R.: Global land cover classification at 1km spatial resolution using a classification tree approach, International Journal of Remote Sensing, 21(6-7):1331 – 1364, DOI:10.1080/014311600210209 https://doi.org/10.1080/014311600210209, 2010.

Harries, J. E., Russell, J. E., Hanafin, J. A., Brindley, H., Futyan, J., Rufus, J., Kellock, S., G. Matthews, R. Wrigley, A. Last, J. Mueller, R. Mossavati, J. Ashmall, E. Sawyer, D. Parker, M. Caldwell, P M. Allan, A. Smith, M. J. Bates, B. Coan, B. C. Stewart, D. R. Lepine, L. A. Cornwall, D. R. Corney, M. J. Ricketts, D. Drummond, D. Smart, R. Cutler, S. Dewitte, N. Clerbaux, L. Gonzalez, A. Ipe,C. Bertrand, A. Joukoff, D. Crommelynck, N. Nelms, D. T. Llewellyn-Jones, G. Butcher, G. L. Smith, Z. P Szewczyk, P E. Mlynczak, A. Slingo, R. P. Allan, and M. A. Ringer: The Geostationary Earth Radiation Budget Project, Bull. Amer. Meteor. Soc. 86 (7): 945, doi: 10.1175/BAMS-86-7-945, 2005.

Isaacs, R. G., W.-C. Wang, R. D. Worsham, and S. Goldenberg, S.: Multiple scattering LOWTRAN and FASCODE models. Applied Optics, 26(7), 1272 – 1281, 1987.

Kato, S., and Loeb, N. G.: Top-of-atmosphere shortwave broadband observed radiance and estimated irradiance over polar regions from Clouds and the Earth's Radiant Energy System (CERES) instruments on Terra, J. Geophys. Res., 110, D07202, doi:10.1029/2004JD005308, 2005.

Laszlo, I., Liu, H., Kim, H.-Y., and Pinker, R. T. : GOES-R Advanced Baseline Imager (ABI) Algorithm Theoretical Basis Document (ATBD) for Downward Shortwave Radiation (Surface), and Reflected Shortwave Radiation (TOA), version 3.1, Available at https://www.goes-r.gov/resources/docs.html, 2018.

Laszlo, I., Liu, H., Kim, H.-Y., and Pinker, R. T.: Shortwave Radiation from ABI on the GOES-R Series, in: *The GOES-R Series,* edited by S. J. Goodman, T. J. Schmit, J. Daniels and R. J. Redmon. 179-191, Elsevier, doi: https://doi.org/10.1016/B978-0-12-814327-8.00015-9, 2020.

Loeb, N. G., Smith, N. M., Kato, S., Miller, W. F., Gupta, S. K., Minnis, P. and Wielicki, B. A.: Angular Distribution Models for Top-of Atmosphere Radiative Flux Estimation from the Mission Satellite, Part I: Methodology, Journal of Applied Meteorology, 42 240-265, 2003.

Loeb N. G. et al.: Angular distribution models for top-of- atmosphere radiative flux estimation from the Clouds and the Earth's Radiant Energy System Instrument on the Terra satellite. part I: Methodology. J. Atmos. Oceanic Technol., 22:338–351, 2005.

Loveland T. R., B. C. Reed, J. F. Brown, D. O. Ohlen, Z. Zhu, L. Yang, J. W. Merchant: Development of a global land cover characteristics database and IGBP DISCover from 1 km AVHRR data, International Journal of Remote Sensing, 21 (6-7), 1303-1330, 2010.

Ma, Y., R. T. Pinker, M. M. Wonsick, C. Li, and L. M. Hinkelman: Shortwave radiative fluxes on slopes. JAMC, 55, 1513-1532, https://doi.org/10.1175/*JAMC*-D-15-0178.1, 2016.

Ma, Y. and Pinker, R. T.: Shortwave Radiative Fluxes from Satellites: An Update. J. Geophys. Res. Atmos**.**, 117, Issue D23, DOI: 10.1029/2012JD018332, 2012.

Niu, X. and Pinker, R. T.: Revisiting satellite radiative flux computations at the top of the atmosphere, International Journal of Remote Sensing, DOI:10.1080/01431161.2011.571298, 2011.

Niu, X. and Pinker, R. T.: An improved methodology for deriving high resolution surface shortwave radiative fluxes from MODIS in the Arctic region, J. Geophys. Res. Atmos., 120, 2382–2393, doi: 10.1002/2014JD022151, 2015.

Pinker, R. T., Zhang B., Dutton E. G.: Do satellites detect trends in surface solar radiation? *SCIENCE*, 308, 5723, 850-854, 2005.

Pinker, R. T., A. Bentamy, B. Zhang, W. Chen, and Ma, Y.: The net energy budget at the ocean-atmosphere interface of the ‘‘Cold Tongue’’ region, J. Geophys. Res. Oceans, 122, doi: 10.1002/2016JC012581, 2017a.

Pinker, R. T., S. Grodsky, B. Zhang, A. Busalacchi, and Chen, W.: ENSO Impact on Surface Radiative Fluxes as Observed from Space. J. Geophys. Res.-Oceans., doi: 10.1002/2017JC012900, 2017b.

Pinker, R. T., Zhang, B. Z., Weller, R. A., and Chen, W.: Evaluating surface radiation fluxes observed from satellites in the southeastern Pacific Ocean. Geophysical Research Letters, 45. https://doi.org/10.1002/2017GL076805, 2018.

Rajulapati, C. R., S. M. Papalexiou, M. P. Clark, and Pomeroy, J. W.: The Perils of Regridding: Examples Using a Global Precipitation Dataset, Journal of Applied Meteorology and Climatology, 60 (11), 1561–1573, doi: 10.1175/JAMC-D-20-0259.1, 2021.

Rilee M. L. and Kuo, K. S.: The Impact on Quality and Uncertainty of Regridding Diverse Earth Science Data for Integrative Analysis, IN43C-0916, 2018.

Scarino et al.: A Web-Based Tool for Calculating Spectral Band Difference Adjustment Factors Derived from SCIAMACHY Hyperspectral Data, IEEE Trans. Geo. Remote Sens., 54, 5, 10.1109/TGRS.2015.2502904, 2016.

Stamnes, K., S.-C. Tsay, W. Wiscombe and K. Jayaweera: Numerically stable algorithm for discrete-ordinate-method radiative transfer in multiple scattering and emitting layered media, Applied Optics, 27 (12), 2502–2509, 1988.

Su, W., Corbett, J., Eitzen, Z., and Liang, L.: Next-generation angular distribution models for top-of-atmosphere radiative flux calculation from CERES instruments: methodology, Atmos. Meas. Tech., 8, 611–632, https://doi.org/10.5194/amt-8-611-2015, 2015.

Wang, H; Pinker, R. T.: Shortwave radiative fluxes from MODIS: Model development and implementation. JGR-Atmospheres, 114, D20201, 2009.

Wielicki, B. A.; Doelling, D. R.; Young, D. F.; Loeb, N. G.; Garber, D. P.; MacDonnell, D. G.: Climate quality broadband and narrowband solar reflected radiance calibration between sensors in orbit. In Proceedings of the IGARSS 2008 IEEE International Geoscience and Remote Sensing Symposium, Boston, MA, USA, 7–11 July 2008.

Zhang, T., Stackhouse Jr., P. W., Cox, S. J., Mikovitz, J. C., Long, C. N.: Clear-sky shortwave downward flux at the Earth's surface: Ground-based data vs. satellite-based data, Journal of Quantitative Spectroscopy & Radiative Transfer, 224, 247-260, 2019, www.elsevier.com/locate/jqsrt.

Tables

Table 1. Channel information and spectral bands for ABI.

ABI Band #	*Central wavelength (μm)*	*Spectral band (μm)*
1	VIS 0.47	0.45-0.49
2	VIS 0.64	0.60-0.68
3	NIR 0.86	0.847-0.882
4	NIR 1.38	1.366-1.380
5	NIR 1.61	1.59-1.63
6	NIR 2.26	2.22-2.27

536

537

538

539 Table 2. Surface classification description for IGBP 18 types, IGBP 12 types, CERES clear sky 6 types,
540 and NTB cloudy sky 4 types

<table>
<tr><th>IGBP (18 types)</th><th>IGBP (12 types)</th><th>CERES clear-sky (6 types)</th><th>NTB cloudy-sky (4 types)</th></tr>
<tr><td>Evergreen Needleleaf</td><td rowspan="2">Needleleaf Forest</td><td rowspan="6">Mod-High Tree/Shrub</td><td rowspan="10">Land</td></tr>
<tr><td>Deciduous Needleleaf</td></tr>
<tr><td>Evergreen Broadleaf</td><td rowspan="2">Broadleaf Forest</td></tr>
<tr><td>Deciduous Broadleaf</td></tr>
<tr><td>Mixed Forest</td><td>Mixed Forest</td></tr>
<tr><td>Closed Shrublands</td><td>Closed Shrub</td></tr>
<tr><td>Woody Savannas</td><td>Woody Savannas</td><td rowspan="6">Low-Mod Tree/Shrub</td></tr>
<tr><td>Savannas</td><td>Savannas</td></tr>
<tr><td>Grasslands</td><td rowspan="3">Grasslands</td></tr>
<tr><td>Permanent Wetlands</td></tr>
<tr><td>Tundra</td></tr>
<tr><td>Croplands</td><td>Croplands</td></tr>
<tr><td>Open Shrublands</td><td>Open Shrub</td></tr>
<tr><td>Urban and Built-up</td><td>Open Shrub</td><td>Dark Desert</td><td rowspan="2">Desert</td></tr>
<tr><td>Bare Soil and Rocks</td><td>Barren and Desert</td><td>Bright Desert</td></tr>
<tr><td>Snow and Ice</td><td>Snow and Ice</td><td>Snow and Ice</td><td>Snow and Ice</td></tr>
<tr><td>Water Bodies</td><td>Ocean</td><td>Ocean</td><td>Water</td></tr>
</table>

541
542
543

Table 3. The various classes for which NTB coefficients are generated.

Parameter	Clear condition	Cloudy condition
Aerosol or cloud type	6 aerosol types (rural, maritime, urban, tropospheric, fog, desert)	3 cloud types (cirrus, stratocumulus, altostratus)
Optical depth (OD)	Typical VIS (km) values for each aerosol types (no OD grid for each aerosol type). Rural: 23, maritime: 23, urban: 5, tropospheric: 50, fog: 0.2, desert: (default VIS for wind speed 10m/s)	Cirrus: [0, 0.8, 1.2, 1.8, 3.2] Stratocumulus: [0, 0.8, 1.2, 1.8, 3.2, 5.8, 8.2, 15.8, 32.2, 51.8, 124.2] Altostratus: [0, 15.0, 30.0, 50.0, 80.0]
Surface type	12 IGBP surface types	4 types (Water, Land, Desert, Snow/Ice)

Table 4. Angles used in simulations. To be consistent with what is presented in the ABI Shortwave Radiation Budget (SRB) Algorithm Theoretical Basis Documents (ATBD) (Laszlo et al, 2018) the additional angles used in the simulations are not given in this Table.

Angle Type	Angles
Solar Zenith Angle [°]	0.0, 12.9, 30.8, 41.2, 48.3, 56.5, 63.2, 69.5, 75.5, 81.4, 87.2
Satellite Zenith Angle [°]	0.0, 11.4, 26.1, 40.3, 53.8, 65.9, 76.3
Azimuth Angle [°]	0.0, 1.9, 10.0, 24.2, 44.0, 68.8, 97.6, 129.3, 162.9, 180

Table 5. MODTRAN simulation speed test (CPU MHz 2099.929).

Algorithm	Stream	Band Resolution (cm^{-1})	Speed (~seconds)
Isaacs	2	1	40
DISORT	2	1, 5, 15	280, 70, 30
	4	1, 5, 15	560, 120, 40
	8	1, 5, 15	930, 300, 110
Scaled Isaac	2	1, 5, 15	30, 10, 6.67
	4	1, 5, 15	30, 10, 6.67
	8	1, 5, 15	30, 10, 6.67

Table 6. Details on data used as input for calculations.

Short Name	Long Name	MODE	ABI-Channel	Scan Sector	Spatial Resolution
RadC	L1b Radiance	M6	C01-C06	CONUS	5000x3000
AODC	L2 Aerosol	M6	--	CONUS	2500x1500
ACMC	L2 Clear Sky Masks	M6	--	CONUS	2500x1500
ACTPC	L2 Cloud Top Phase	M6	--	CONUS	2500x1500
CODC*	L2 Cloud Optical Depth	M6	--	CONUS	2500x1500

*The CODC data were not always available from CLASS and had to be obtained from NOAA/STAR temporary archives. Also, not all the required angular information needed for implementation of the regressions is available online and had to be re-generated.

570 Table 7. Statistical summary for all selected cases inter-compared at instantaneous time scale.

Case	CERES	GOES-R	Corr	Bias	Std	RMSE	N
07/31 2019 UTC 19	Terra	G16	0.82	0.81	69.81	69.81	0.22 x10^6
		G17	0.87	29.13	90.10	94.70	1.78 x10^6
	Aqua	G16	0.76	33.87	117.43	122.22	1.58 x10^6
		G17	0.78	31.53	129.42	133.21	0.29 x10^6
09/13 2019 UTC 20	Terra	G16	0.87	-17.37	81.72	83.54	0.13x10^6
		G17	0.71	47.09	108.73	118.48	1.73x10^6
	Aqua	G16	0.76	18.22	108.50	110.02	1.46x10^6
		G17	0.73	25.14	81.95	85.72	0.53x10^6
09/21 2019 UTC 19	Terra	G16	0.85	6.78	66.66	67.00	0.35x10^6
		G17	0.83	26.41	87.64	91.57	1.75x10^6
	Aqua	G16	0.82	29.66	105.09	109.20	1.67x10^6
		G17	0.76	6.03	94.70	94.89	0.15x10^6
09/30 2019 UTC 19	Terra	G16	0.88	4.49	64.79	64.94	0.40x10^6
		G17	0.80	19.35	86.41	88.55	1.74x10^6
	Aqua	G16	0.80	19.87	100.45	102.40	1.69x10^6
		G17	0.72	2.71	91.79	91.83	0.12x10^6
	Terra	G16	0.86	5.84	51.44	51.77	0.35x10^6

10/23 2019 UTC 19	Aqua	G17	0.87	22.47	70.25	73.76	$1.75x10^6$
		G16	0.89	17.10	75.95	77.85	$1.67x10^6$
		G17	0.78	8.98	72.52	73.07	$0.15x10^6$
11/08 2019 UTC 19	Terra	G16	0.87	-0.50	43.28	43.28	$0.35x10^6$
		G17	0.82	17.18	71.27	73.31	$1.75x10^6$
	Aqua	G16	0.90	10.08	71.27	71.98	$1.67x10^6$
		G17	0.68	1.53	47.55	47.58	$0.15x10^6$
11/24 2019 UTC 19	Terra	G16	0.79	7.98	49.10	49.75	$0.35x10^6$
		G17	0.87	14.10	78.35	79.61	$1.76x10^6$
	Aqua	G16	0.82	7.63	58.68	59.17	$1.67x10^6$
		G17	0.65	0.19	63.14	63.14	$0.15x10^6$
12/26 2019 UTC 19	Terra	G16	0.88	5.24	53.28	53.54	$0.35x10^6$
		G17	0.76	11.26	73.95	74.80	$1.76x10^6$
	Aqua	G16	0.83	9.79	58.90	59.56	$1.67x10^6$
		G17	0.73	0.85	52.53	52.54	$0.15x10^6$

List of Figures

Figure 1. Flowchart of the NTB transformations illustrating the main processing sections.
Figure 2. Schematic illustration of the logic employed to synthesize modeled and observed ADMs.
Figure 3. The location of the 100 selected clear sky profiles from SeeBor used in the simulations.
Figure 4. Profile statistics of: (a) temperature; (b): water vapor; (c) ozone for the entire available sample and for the reduced sample used in this study. Error bar is 1 standard deviation.
Figure 5. Re-mapped IGBP surface classifications over the CONUS at 2-km ABI grid.
Figure 6. Simulated Radiances from DISORT 8-stream (with 1, 5, and 15 cm^{-1} resolution band model for spectral range of 0.4 – 0.5 μm (left) and 1.5 – 2.0 μm (right).
Figure 7. Radiance differences between various multi-scattering algorithms and DISORT-8 stream. *Upper*: the whole simulated spectrum of 0.2-4 μm; *Lower:* zoom on 0.3-0.35 μm (Relative Azimuthal Angle=1.9^o, View Angle=76.3^o, Solar Zenith Angle=87.2^o).
Figure 8. Locations of the six ABI channel SRFs. X-axis is wavenumber. Y-axis is solar irradiance.
Figure 9. Comparison of TOA flux from ABI and CERES FLASHFlux for 2017/11/25, 17:57Z. (a) CERES Terra product; (b): results with "separate-channel" coefficients. (c): difference (ABI-CERES); (d): histogram of ABI-CERES differences (this is the only case illustrated in this paper with data from FLASHFlux)
Figure 10. Statistics for relative Bias and RMSE. The y-axis is percentage. The x-axis is the case used in the inter-comparison. Blue - cloudy orange - clear sky and t gray - all sky.
Figure 11. (a) All sky TOA SW from CERES_SSF/Aqua, (b) CERES_SSF/Terra, (c) re-gridded CERES_SSF/Aqua, (d) re-gridded CERES_SSF/Terra, (e) GOES-16 and (f) GOES-17 on 12/26/2019 at UTC 19:36.
Figure 12. (a) Frequency distribution of all-sky TOA SW differences between ABI on GOES-16 and CERES, (b) ABI on GOES-17 and CERES_SSF using Aqua (Upper) and Terra (Lower). All observations were used (clear and cloudy) on 12/26/2019 at UTC 19:36.
Figure 13. Same as Figure 11 but for clear TOA SW differences.

Figure 14. Same as Figure 11 but for cloudy TOA SW differences.

Figure 15. *Left:* Sensor response function for ABI channel 6; *Right:* Spectral albedo for desert and open shrubs. Desert albedo value is much higher than open shrubs at 2.2 μm.

Figures

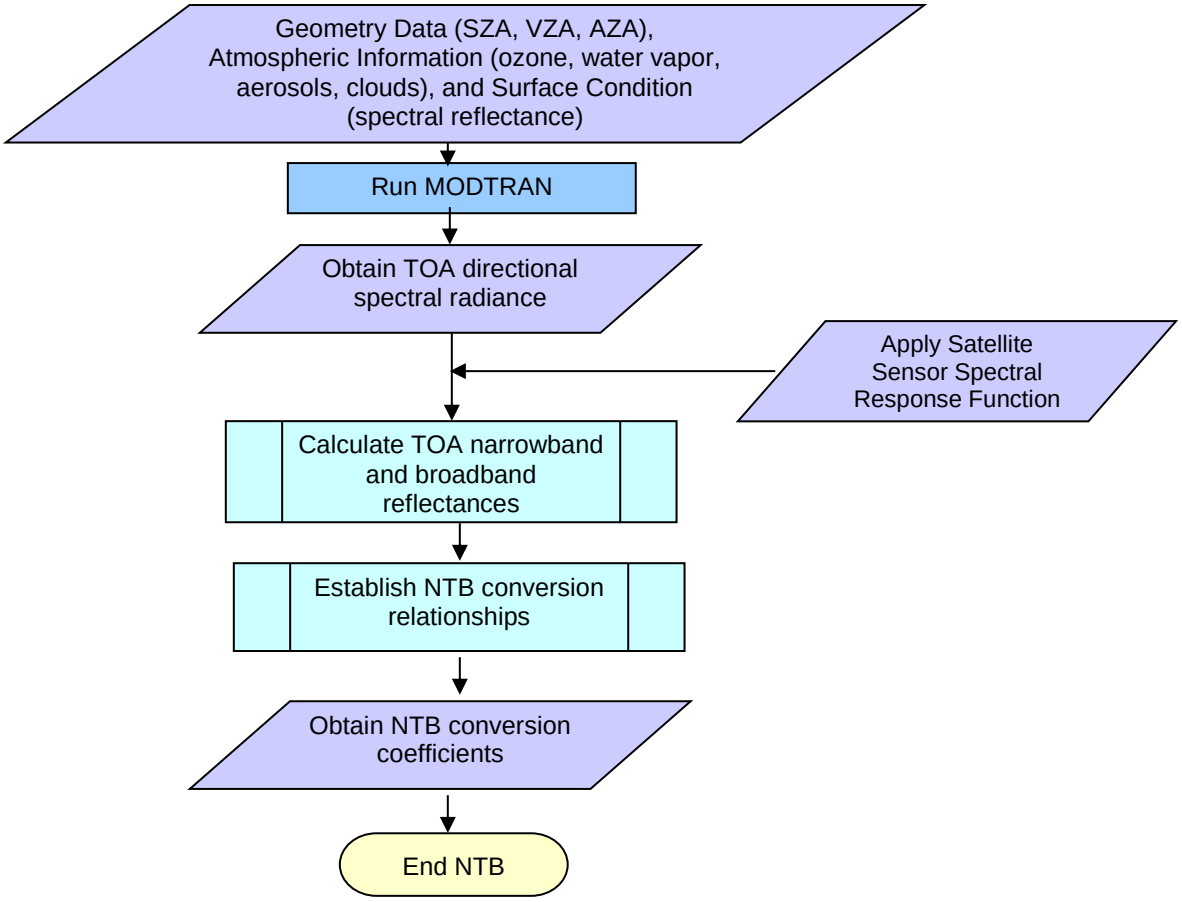

Figure 1. Flowchart of the NTB transformations illustrating the main processing sections.

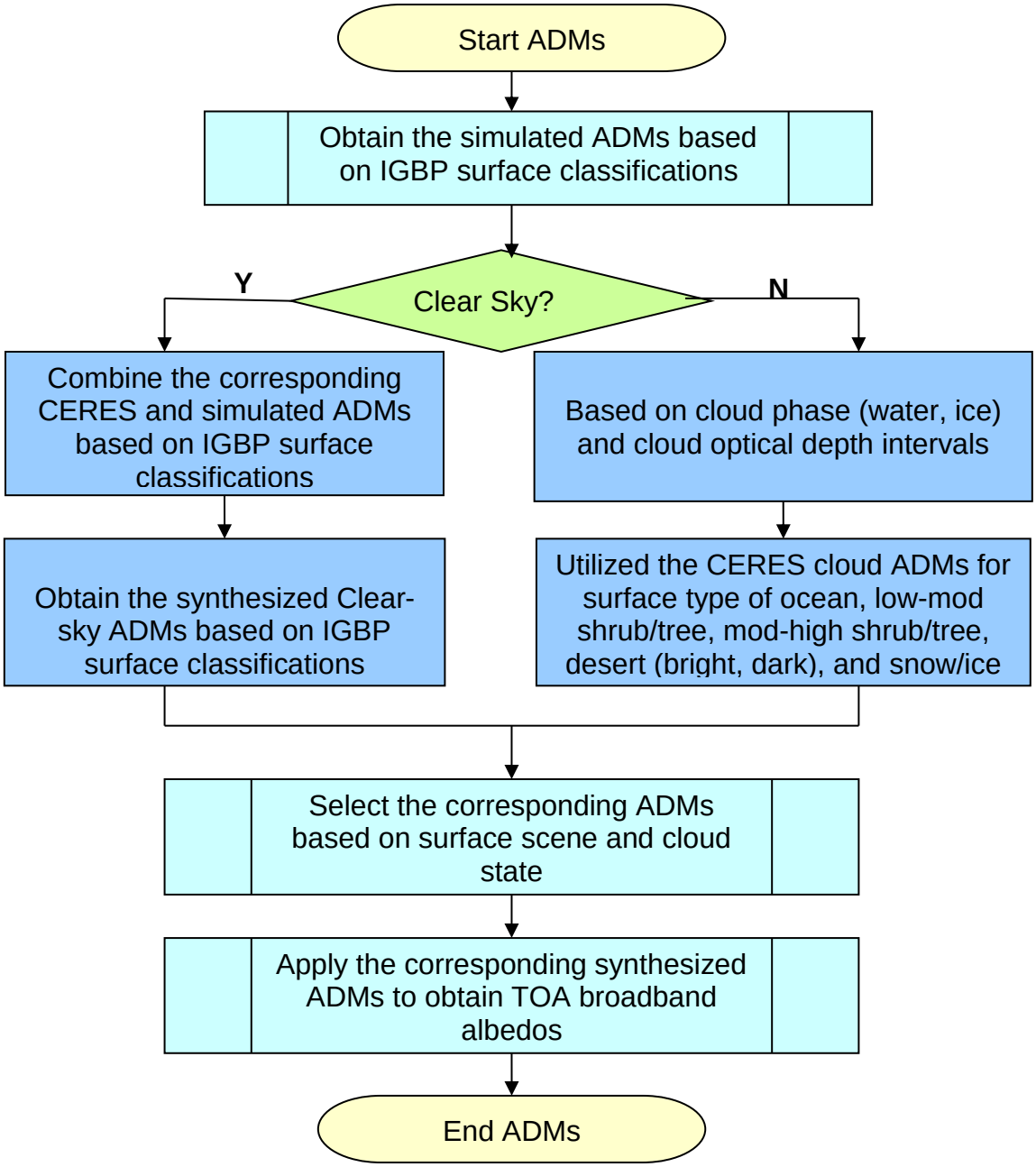

651

652 Figure 2. Schematic illustration of the logic employed to synthesize modeled and observed ADMs.

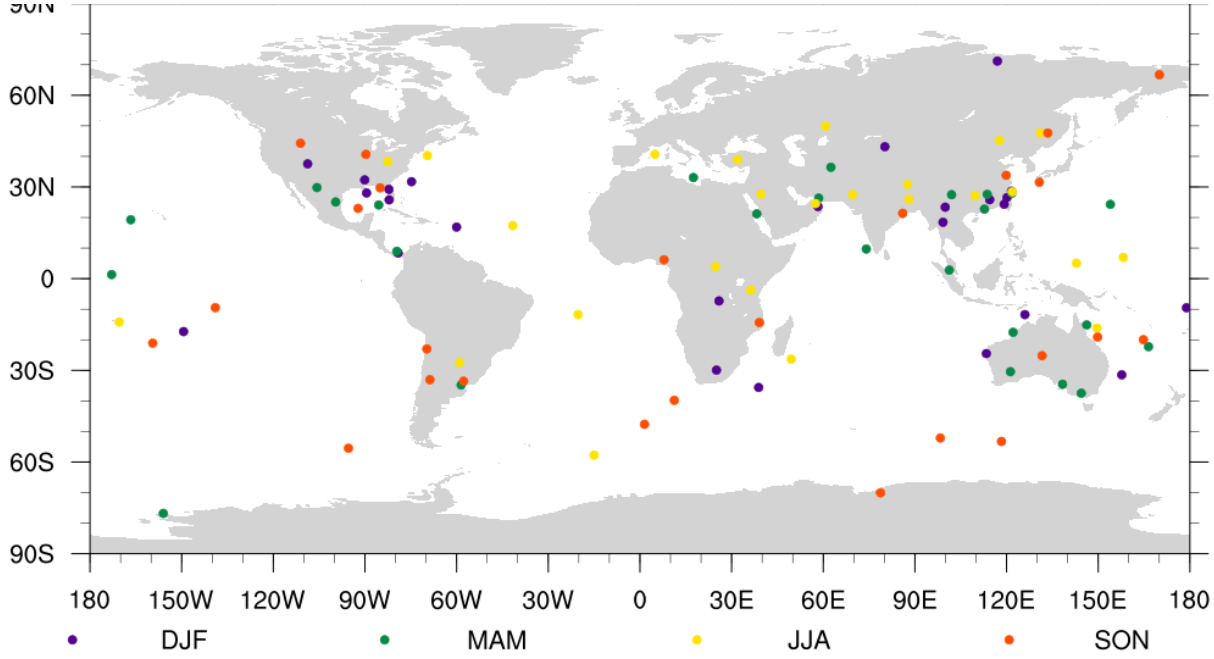

Figure 3. The location of the 100 selected clear sky profiles from SeeBor used in the simulations.

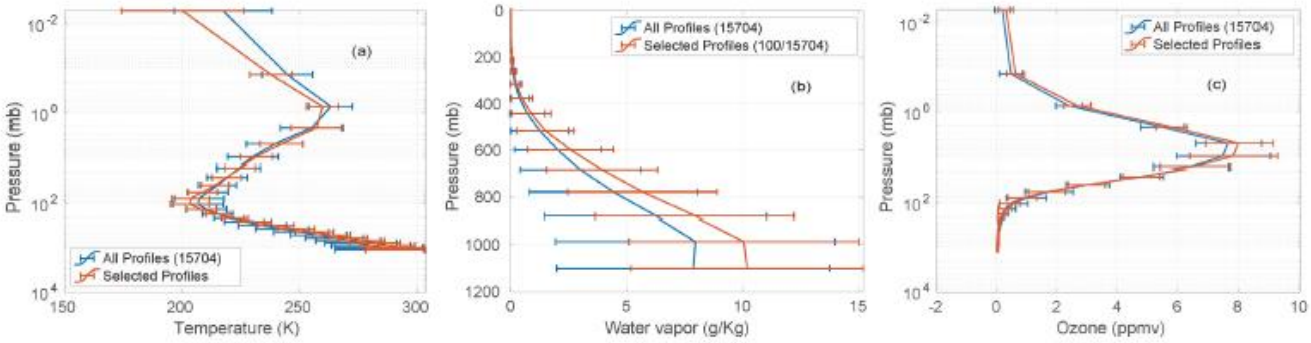

Figure 4. Profile statistics of: (a) temperature; (b): water vapor; (c) ozone for the entire available sample and for the reduced sample used in this study. Error bar is 1 standard deviation.

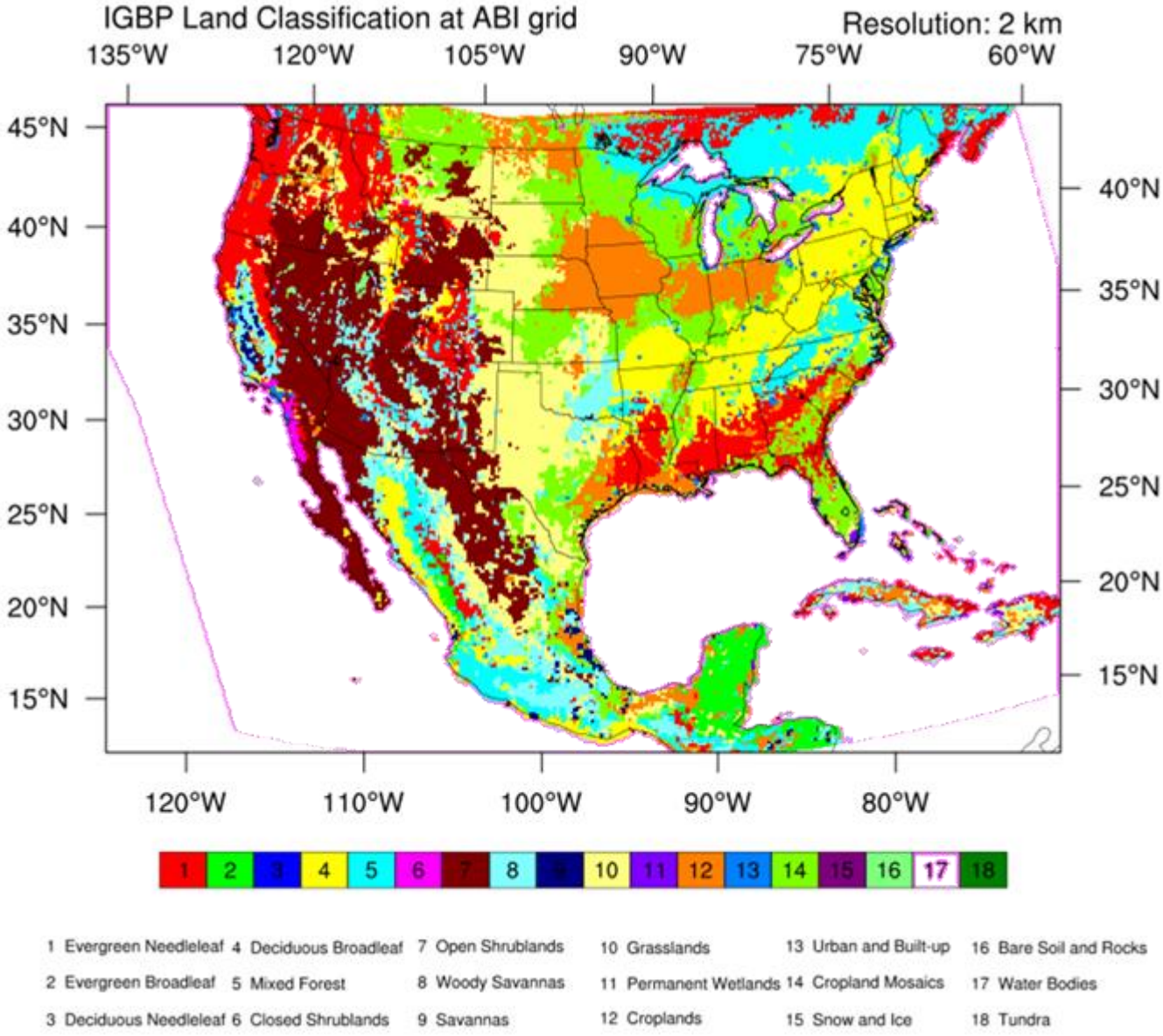

Figure 5. Re-mapped IGBP surface classifications over the CONUS at 2-km ABI grid.

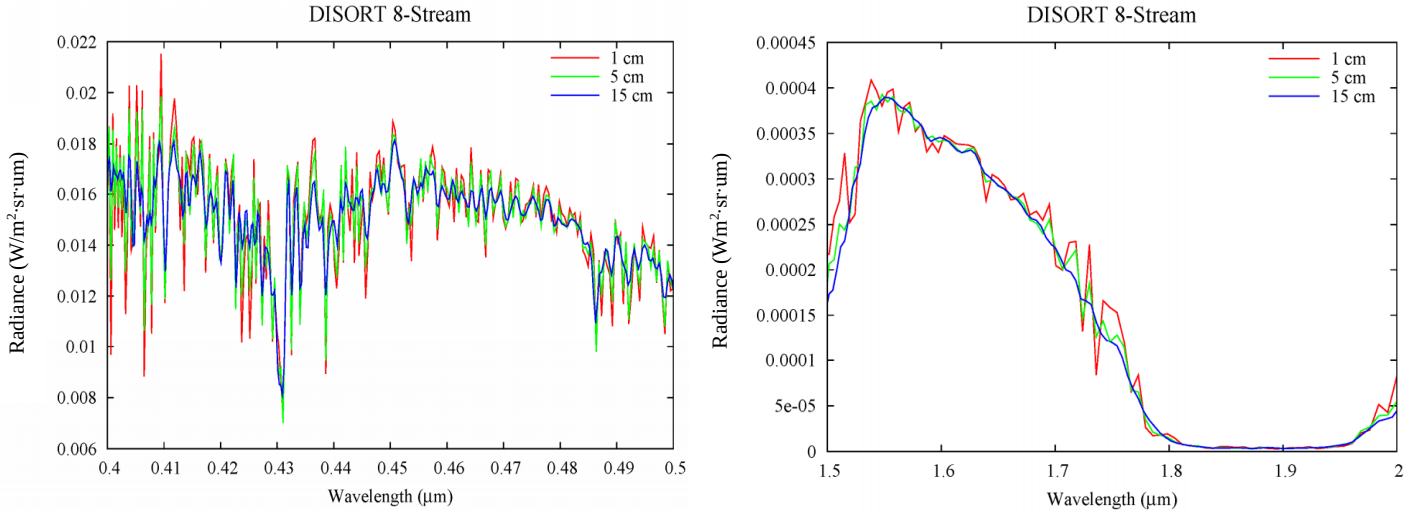

Figure 6. Simulated Radiances from DISORT 8-stream (with 1, 5, and 15 cm^{-1} resolution band model for spectral range of 0.4 – 0.5 µm (left) and 1.5 – 2.0 µm (right).

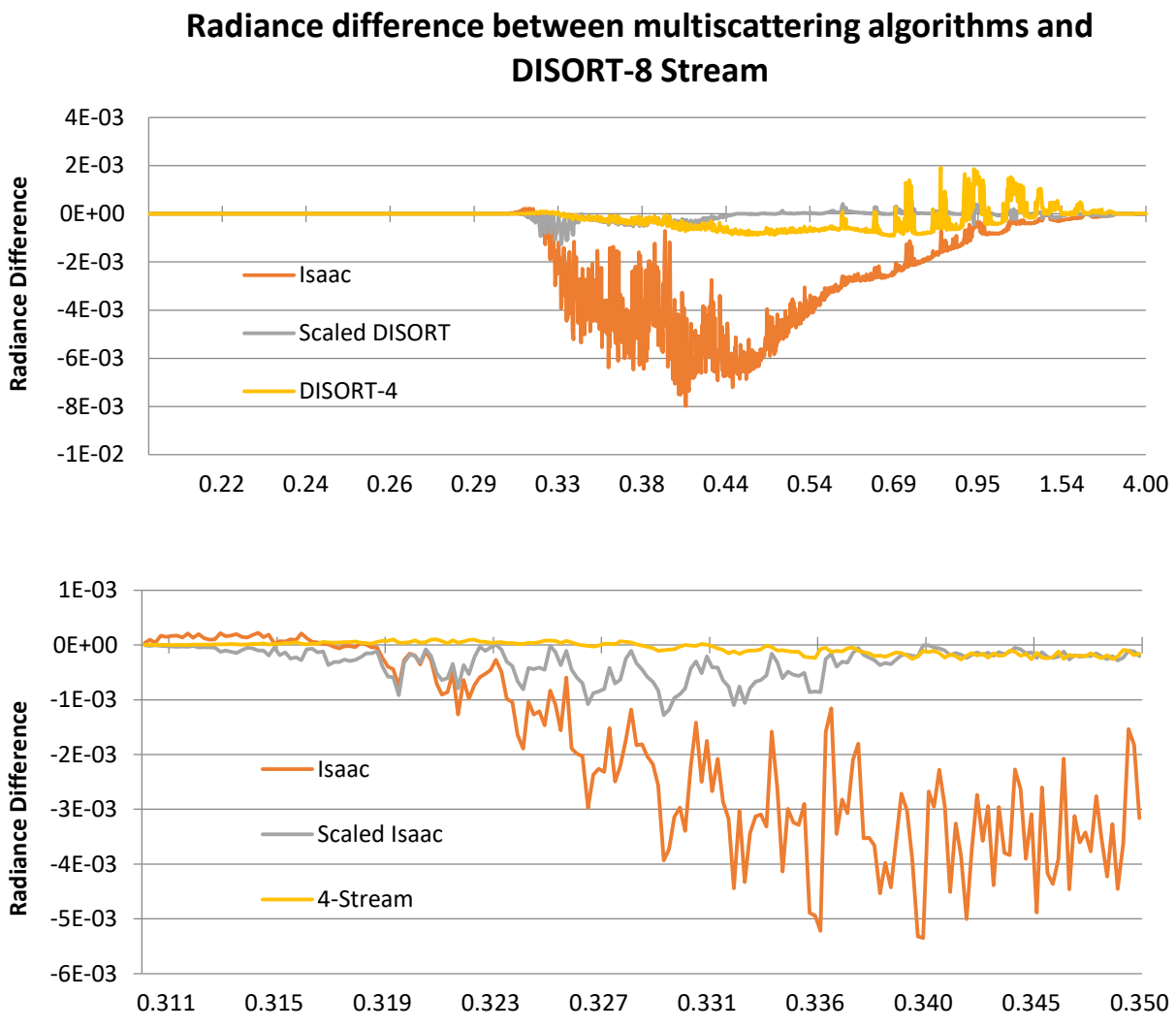

Figure 7. Radiance differences between various multi-scattering algorithms and DISORT-8 stream. *Upper*: the whole simulated spectrum of 0.2-4 μm; *Lower:* zoom on 0.3-0.35 μm (Relative Azimuthal Angle=1.9º, View Angle=76.3º, Solar Zenith Angle=87.2º).

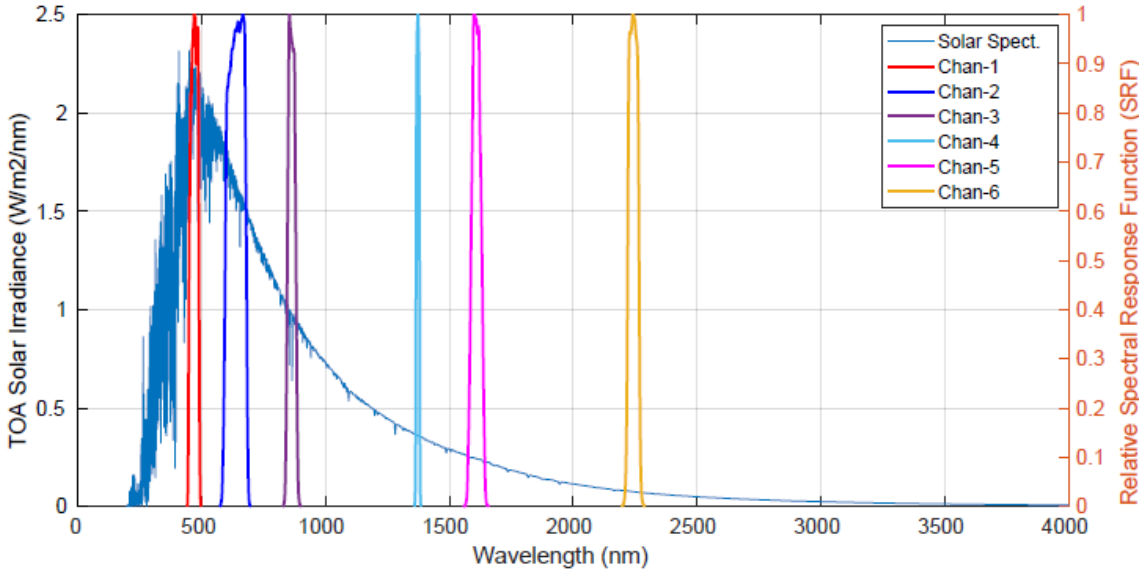

685

686

687 Figure 8. Locations of the six ABI channel SRFs. X-axis is wavenumber. Y-axis is solar irradiance.

688
689

690

691

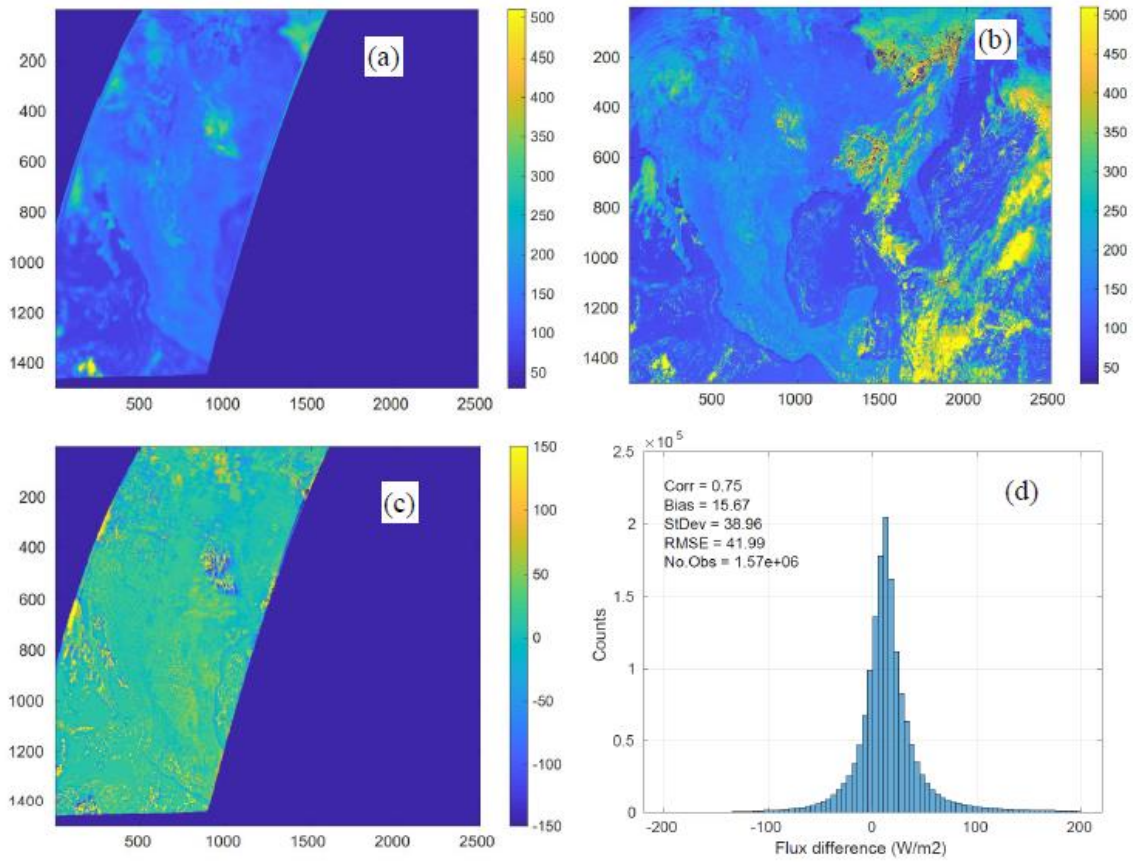

Figure 9. Comparison of TOA flux from ABI and CERES FLASHFlux for 2017/11/25, 17:57Z. (a) CERES Terra product; (b): results with "separate-channel" coefficients. (c): difference (ABI-CERES); (d): histogram of ABI-CERES differences (this is the only case illustrated in this paper with data from FLASHFlux).

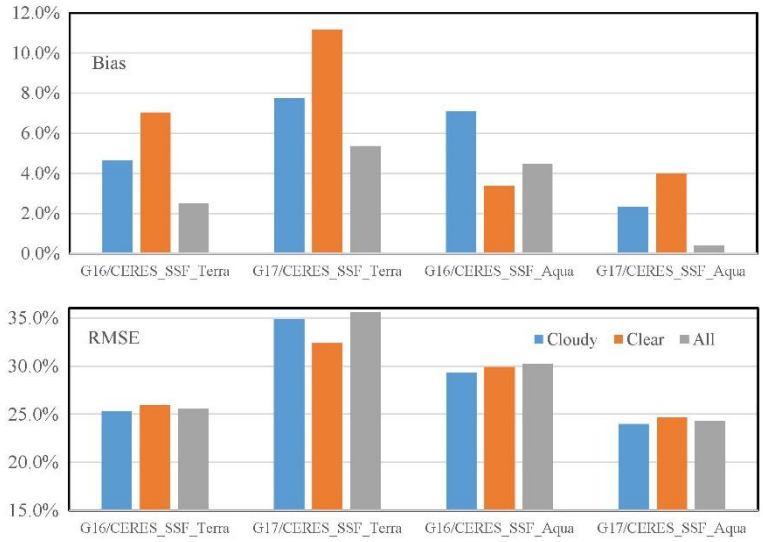

Figure 10. Statistics for relative Bias and RMSE. The y-axis is percentage. The x-axis is the case used in the inter-comparison. Blue - cloudy orange - clear sky and t gray - all sky.

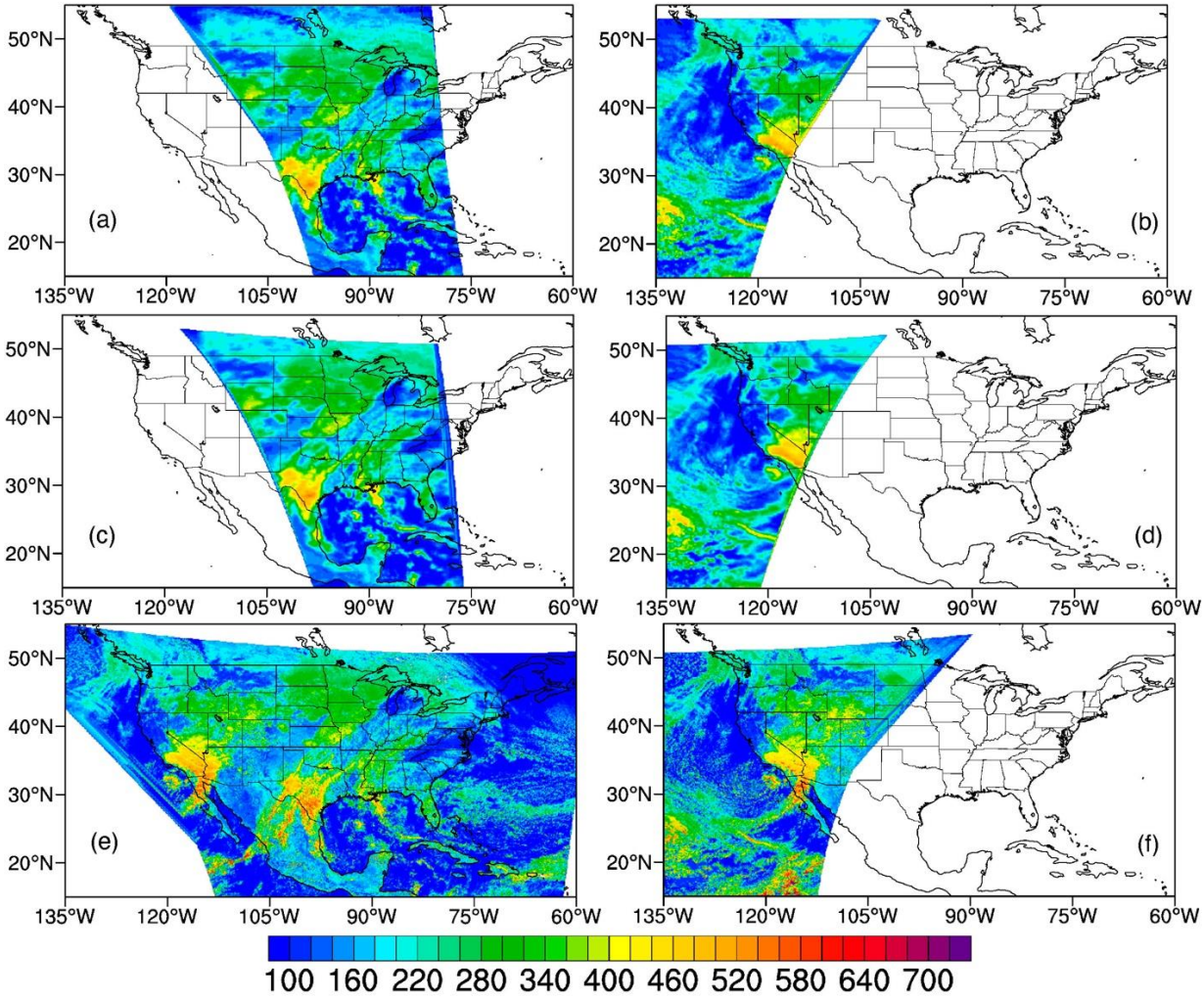

Figure 11. (a) All sky TOA SW from CERES_SSF/Aqua, (b) CERES_SSF/Terra, (c) re-gridded CERES_SSF/Aqua, (d) re-gridded CERES_SSF/Terra, (e) GOES-16 and (f) GOES-17 on 12/26/2019 at UTC 19:36.

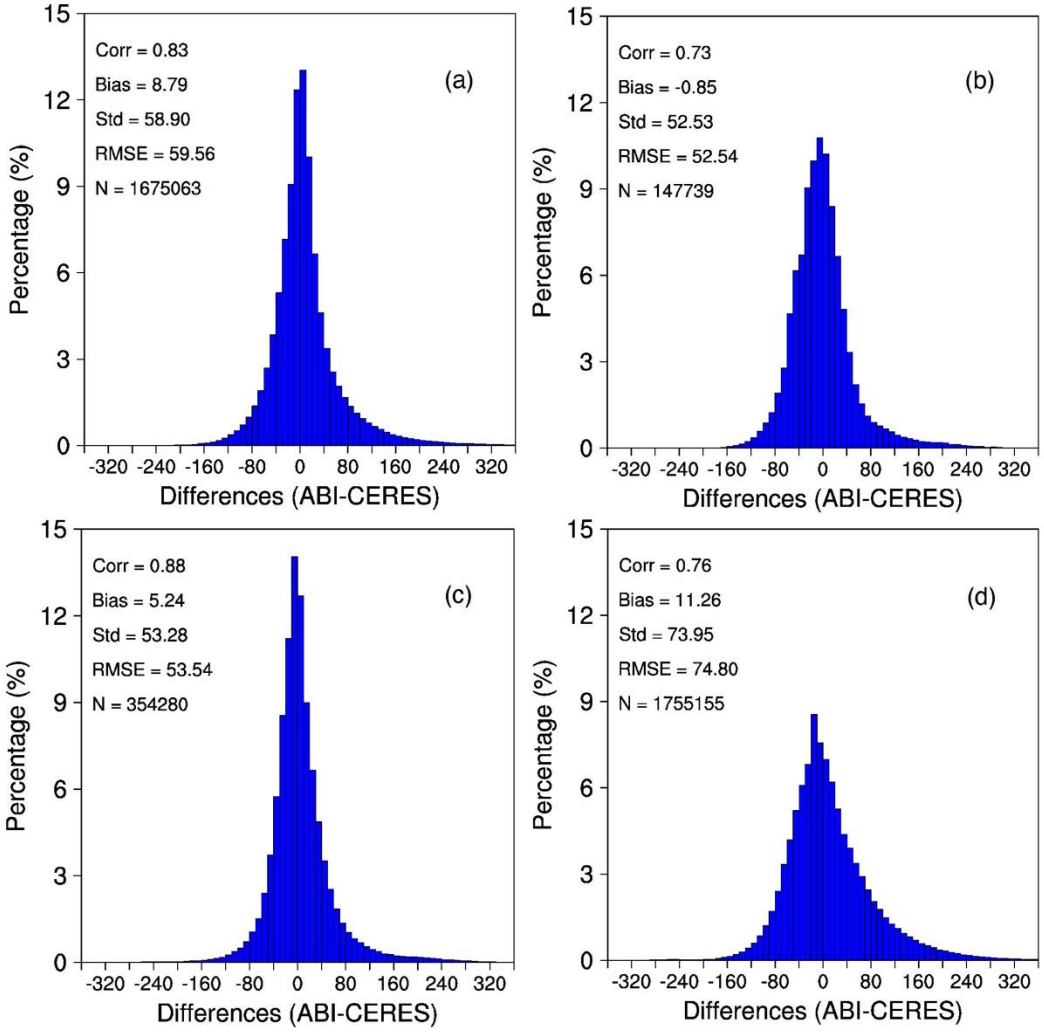

Figure 12. (a) Frequency distribution of all-sky TOA SW differences between ABI on GOES-16 and CERES, (b) ABI on GOES-17 and CERES_SSF using Aqua (Upper) and Terra (Lower). All observations were used (clear and cloudy) on 12/26/2019 at UTC 19:36.

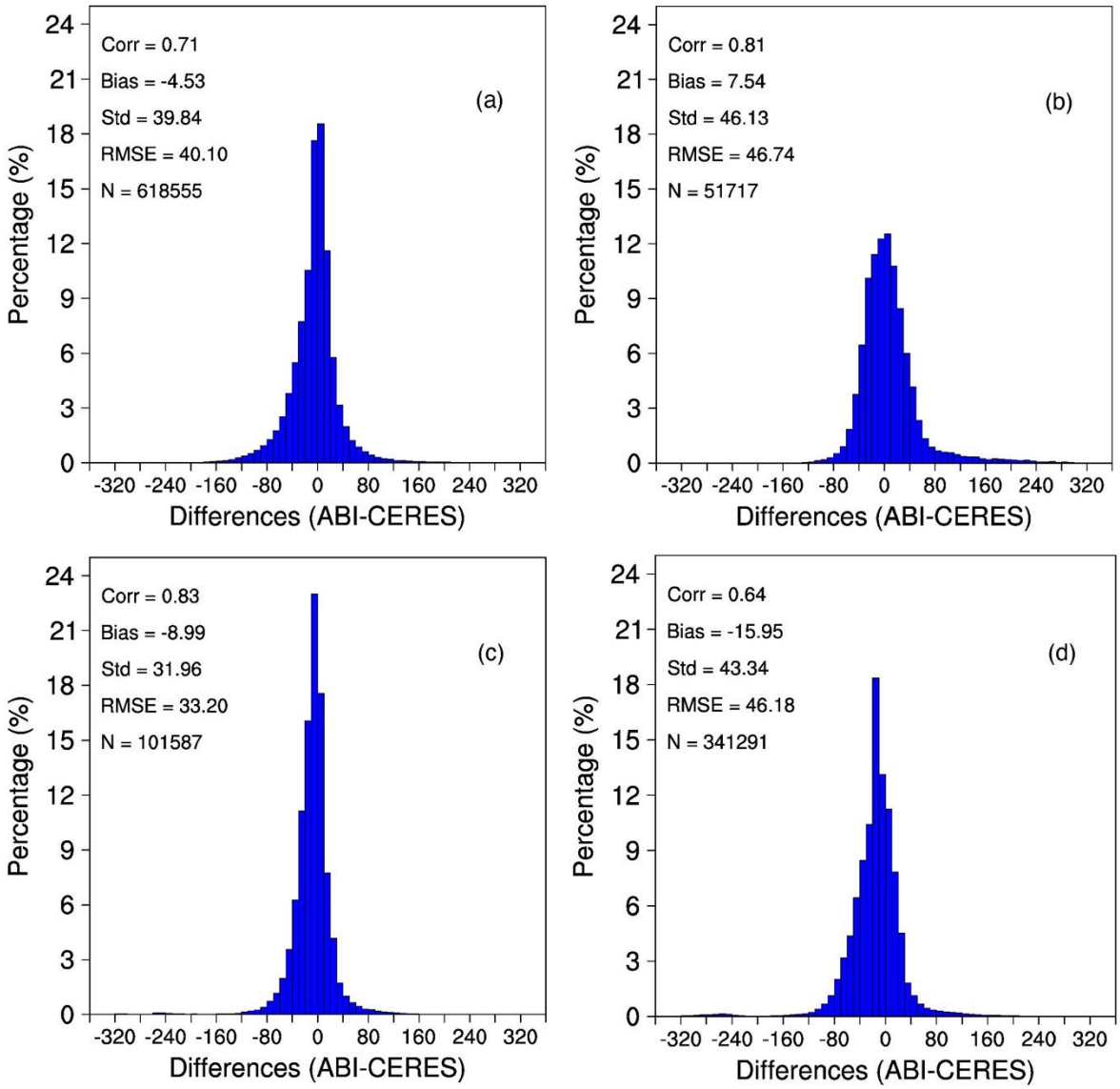

Figure 13. Same as Figure 11 but for clear TOA SW differences.

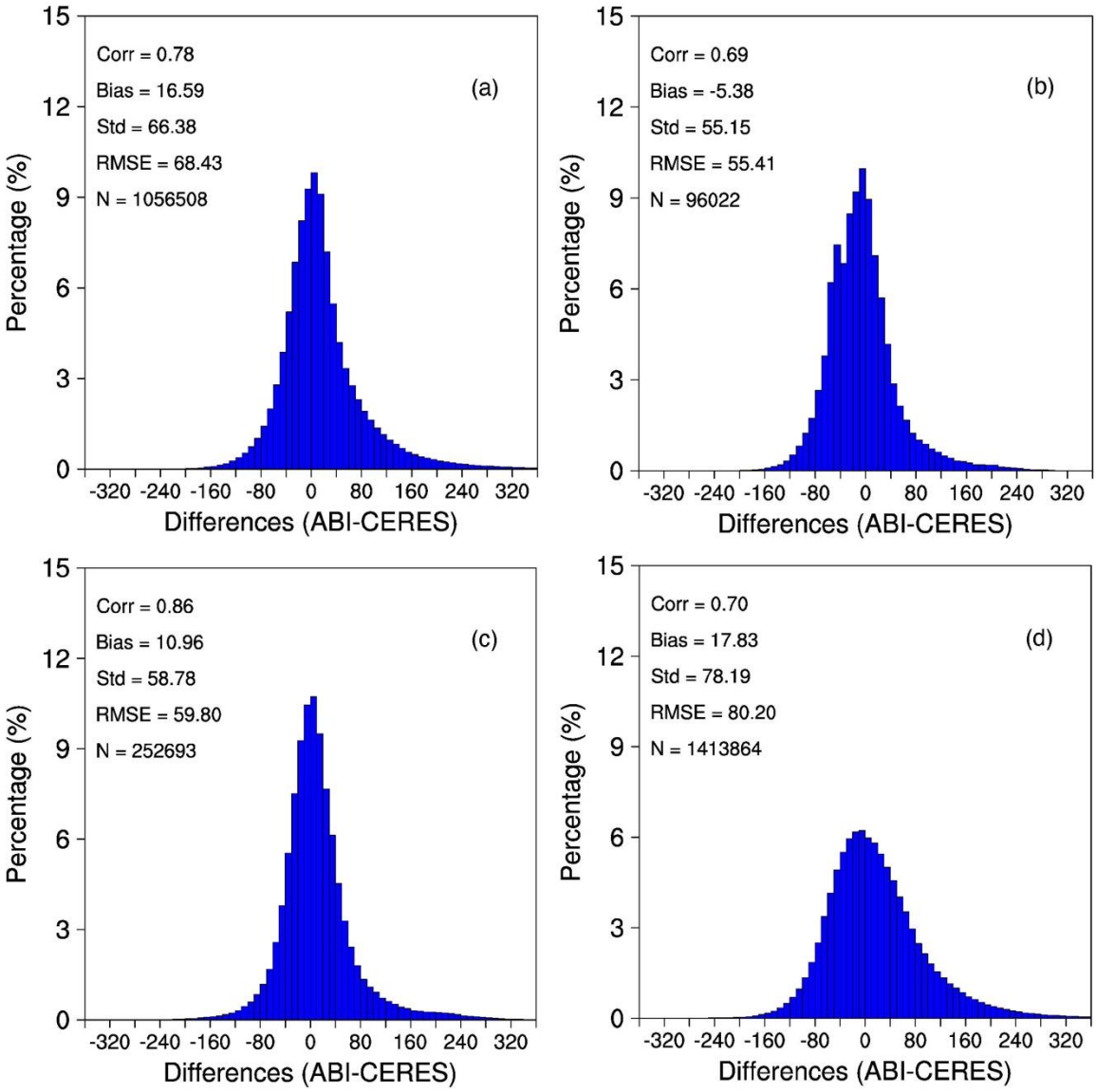

730
731 Figure 14. Same as Figure 11 but for cloudy TOA SW differences.

732
733

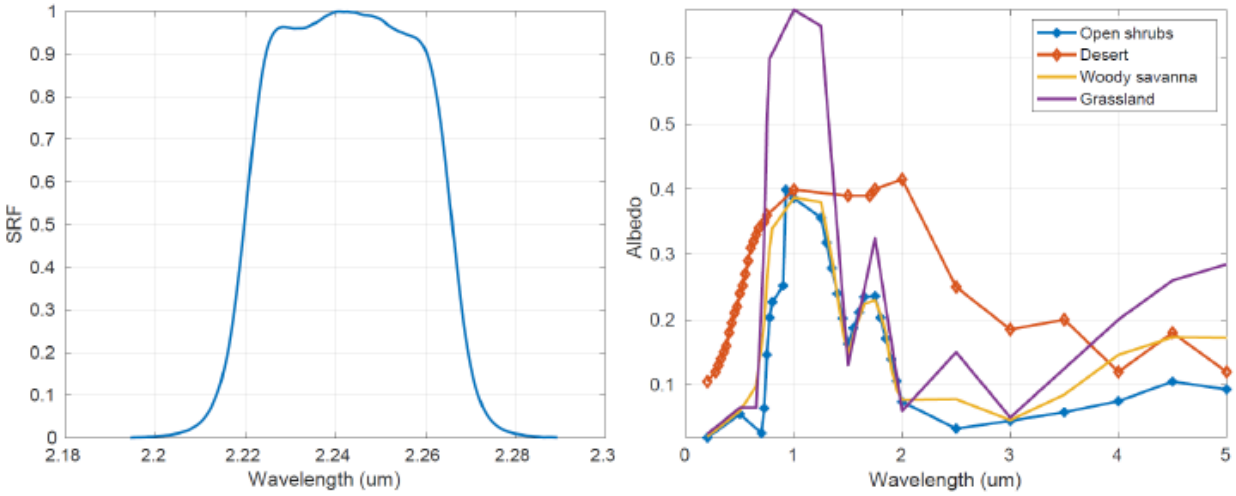

Figure 15. *Left:* Sensor response function for ABI channel 6; *Right:* Spectral albedo for desert and open shrubs. Desert albedo value is much higher than open shrubs at 2.2 µm.